Near-surface physics during convection affecting air-water gas transfer

Near-surface physics during convection affecting air-water gas transfer

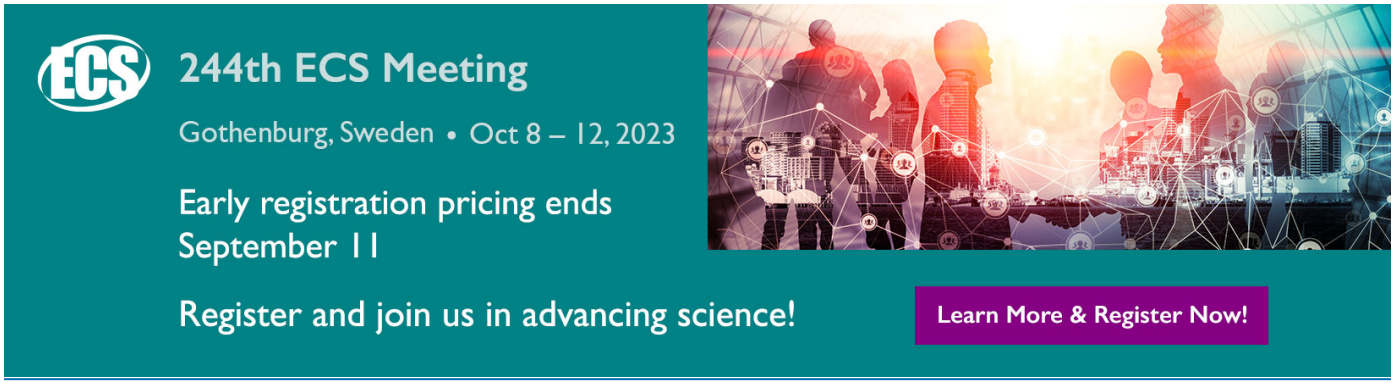

Near-surface physics during convection affecting air-water gas transfer

S T Fredriksson[1], L Arneborg[1], H Nilsson[2] and R A Handler[3]
[1] Department of Marine Sciences, University of Gothenburg, P.O. Box 460, 405 30 Gothenburg, Sweden
[2] Department of Applied Mechanics, Fluid Dynamics, Chalmers University of Technology, 412 96 Gothenburg, Sweden
[3] Department of Mechanical Engineering, Texas A&M University, TX 77843-3123, USA

E-mail: sam.fredriksson@gu.se

Abstract. The gas flux at the water surface is affected by physical processes including turbulence from wind shear, microscale wave breaking, large-scale breaking, and convection due to heat loss at the surface. The main route in the parameterizations of the gas flux has been to use the wind speed as a proxy for the gas flux velocity, indirectly taking into account the dependency of the wind shear and the wave processes. The interest in the contributions from convection processes has increased as the gas flux from inland waters (with typically lower wind and sheltered conditions) now is believed to play a substantial role in the air-water gas flux budget. The gas flux is enhanced by convection through the mixing of the mixed layer as well as by decreasing the diffusive boundary layer thickness. The direct numerical simulations performed in this study are shown to be a valuable tool to enhance the understanding of this flow configuration often present in nature.

1. Introduction

The gas flux, F_g, across the air-water interface is often estimated as

$$F_g = k_g(C_w - \vartheta C_a), \tag{1}$$

where k_g is the gas transfer velocity, C_w and C_a are the gas concentrations in water and air, respectively (Figure 1a), and ϑ is the Ostwald solubility coefficient [1]. F_g is affected by several physical processes, e.g., interfacial shear due to wind forcing, microscale wave breaking at moderate wind speeds, bubbles, raindrops, breaking waves at high wind speeds, and convection due to surface heat loss [2]. k_g is frequently parameterized by empirical models based on the wind speed only. It is apparent that the wind speed, although contributing to many of these processes, is not enough to capture all the processes involved. This is especially true for low wind and zero-wind conditions where different wind speed parameterizations yield a large spectrum of gas transfer velocities ranging from zero upwards [1]. The gas flux during these conditions has received increasing interest since recent global model estimates suggest that inland waters, where low-wind conditions are more frequent than in the oceans, are considerable sources of greenhouse gases. The inland-water source, estimated to be 1 Pg C yr^{-1} [3-5], is of the same magnitude as the ocean net sink, which is estimated to be 1.6 Pg C yr^{-1} [4]. The present

paper qualitatively discusses the gas flux dependency of natural convection during zero-wind conditions while Fredriksson et al. [6] present a more thorough method discussion and quantitative results.

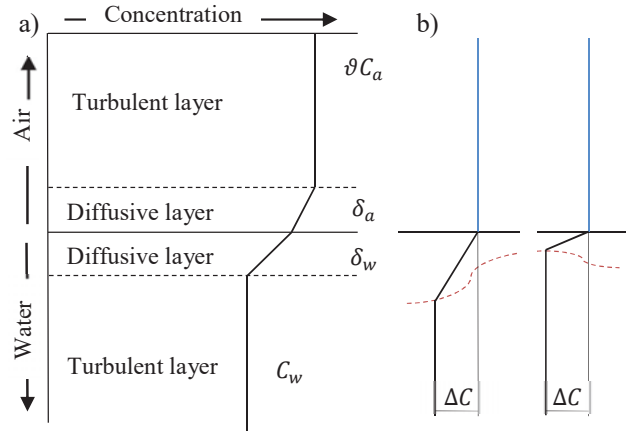

Figure 1. a) Conceptual diagram [1] of the mean gas concentration for a general gas without chemically enhanced diffusion in the water, the turbulent layers where advective transport dominates, and the boundary layers where diffusive transport dominates. b) Two snapshots of gas concentrations, assuming small gas concentration gradients in the air, and varying water diffusive boundary layer depths due to natural convection.

2. Modelling of air-water gas transfer

This study models the transport of a dissolved gas using a passive scalar in direct numerical simulations (DNS) of fully developed turbulent natural convective flow in the surface layer of oceans or lakes (Figure 2). The gas exchange across an air-water interface is affected by biochemical and physical factors. Biochemical factors, not considered in this study, are typically chemical or biological processes that produce or consume gas. Physical factors include advective and diffusive transport (Figure 1). For the water side, the advective motions dominate the transport of gas from the deeper water masses up to the diffusive sublayer, in which the vertical motions are attenuated and the molecular diffusion eventually takes over close to the surface. The actual gas exchange across the air-water interface is then, when bubbles or raindrops are not present, maintained by molecular diffusion driven by the air-water gas concentration gradient. The gas concentration gradients for CO_2 and CH_4 (typical greenhouse gases) are controlled by the water side [7], which allows studies of the exchange dynamics to be performed in the aqueous phase only. The horizontal gas concentration gradients for these gases are further assumed to be much smaller in the air than in water because the molecular diffusivities are several magnitudes higher in the air than in the water [8]. Hence a constant concentration boundary condition for the gas is imposed from the air side. The often used illustration of a constant gradient diffusive layer above a constant concentration layer (Figure 1a) is a rather coarse representation of the averaged quantities, not to speak about the momentary profiles. In reality the momentary concentration profiles show large variations of the diffusive layer thickness, and thereby also of the gradients and surface fluxes (Figure 1b). DNS is here used as a very valuable tool to study the momentary flow field sketched in Figure 1b in order to actually understand the processes that drive the flow and the gas transfer.

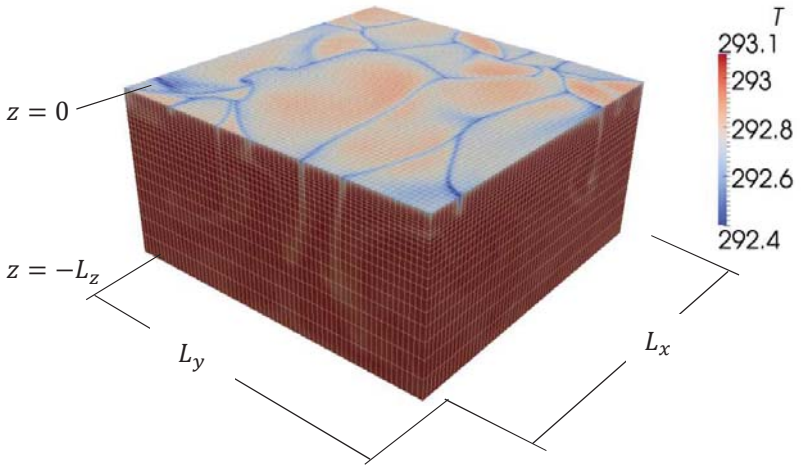

Figure 2. Computational domain, representing the surface layer of oceans or lakes. The mesh is equidistant in the x- and y-direction and graded in the z-direction. Every fourth mesh line in each direction is shown here. The constant surface heat flux cools the surface water and forms thin plumes of cold denser water moving downwards.

3. Governing equations, discretization, numerical cases, and statistical sampling

The flow is governed by the Navier-Stokes equations, which under the Boussinesq approximation [9] can be written as

$$\frac{\partial \boldsymbol{u}}{\partial t} + \boldsymbol{u} \cdot \nabla \boldsymbol{u} = -\frac{1}{\rho_0}\nabla P + \upsilon \nabla^2 \boldsymbol{u} + \beta\,(T - T_0)\boldsymbol{g}, \tag{2}$$

$$\nabla \cdot \boldsymbol{u} = 0, \tag{3}$$

and the thermal energy equation

$$\frac{\partial T}{\partial t} + \boldsymbol{u} \cdot \nabla T = \alpha \nabla^2 T + \phi_T. \tag{4}$$

Here $\boldsymbol{u} = (u, v, w)$ is the velocity vector where u, v are in the lateral directions and w is in the surface-normal direction. t is the time, υ is the kinematic viscosity of water, and P is a modified pressure with the background hydrostatic pressure for the constant density ρ_0 subtracted. β is the coefficient of thermal expansion, T is the temperature, T_0 is the reference temperature, and $\boldsymbol{g}$ is the gravitational acceleration. α is the thermal diffusivity and ϕ_T is a spatially and temporally constant source term added to maintain a constant mean temperature in the domain. The transport of the passive scalar s used to model the dissolved gas is governed by

$$\frac{\partial s}{\partial t} + \boldsymbol{u} \cdot \nabla \mathrm{s} = D \nabla^2 s + \phi_s, \tag{5}$$

where $\phi_s = F_s/L_z$ is a spatially evenly distributed and temporally constant source term given by the scalar flux F_s through the top boundary and the domain depth L_z.

The domain is a non-deformable rectangular box, assuming that the deflection of the surface (top boundary) is negligible. The surface and bottom boundaries are assumed to be shear-free and the slip boundary condition $\partial u/\partial z = \partial v/\partial z = w = 0$ is applied on both. The surface heat flux is, during natural convection with no wind, dominated by long-wave radiation, which is assumed to be constant in the present simulations resulting in a constant gradient surface temperature boundary condition $\partial T/\partial z = -Q/\lambda$. Here $Q > 0$ is a constant heat flux directed out of the surface boundary, $\lambda = \rho c_p \alpha$ is the thermal conductivity, and c_p is the specific heat capacity. The scalar concentration at the surface is assumed to be constant $s = S_0$. The bottom boundary is assumed to be adiabatic and without scalar exchange with the lower water masses, i.e., $\partial T/\partial z = \partial s/\partial z = 0$. Finally, periodic boundary conditions are applied at the sides.

3.1. Discretization

The governing equations are solved using a collocated finite volume approach using the OpenFOAM open-source computational fluid dynamics code. The diffusion and advection terms are discretized using the second-order central differencing scheme and the time derivative is discretized using the Crank-Nicolson scheme [10]. The time step Δt is dynamically adjusted to keep the Courant-Friedrich-Lewy number (CFL) less than 0.5 in all cells. This typically gives a time step much smaller than the Kolmogorov time scale, and is therefore the limiting constraint for the time step.

The aspect ratios of the domain are $L_x = L_y = 2L_z$ and the mesh resolution is $256 \times 256 \times 96$ for all simulations. The mesh is graded in the vertical direction (Figure 2), where the distances between the center of the first cell to the bottom and surface boundary are 1.96 mm and 0.098 mm, respectively. The results presented in Fredriksson et al. [6] support the assumption that the current vertical and lateral dimensions of the domain are large enough to give representative results for the surface mixed layer although the dimensions are much smaller than in reality. The same study further concludes, via an extensive mesh resolution study, that the mesh resolution is appropriate to resolve the flow field at hand.

3.2. Numerical simulations

Three simulations are presented. The surface heat flux is varied as one *Base* case with a dimensional heat flux of $100\ \mathrm{Wm}^{-2}$ ($Ra = 5 \cdot 10^8$), as well as one *Low* case ($50\ \mathrm{Wm}^{-2}$, $Ra = 2.5 \cdot 10^8$), and one *High* case ($200\ \mathrm{Wm}^{-2}$, $Ra = 10 \cdot 10^8$). Here $Ra = \beta g Q L^4 / \alpha \upsilon \lambda$ is the Rayleigh number using standard molecular properties for water at room temperature. The characteristic length, L, is here chosen as the domain depth $L_z = 0.1204\ m$. The Prandtl number, $Pr = \upsilon/\alpha$, and the Schmidt number, $Sc = \upsilon/D$, are 7 for all cases.

3.3. Statistical sampling

The sampling of the statistical properties of the turbulent fluctuations is done under fully developed conditions, defined by steady mean ($\bar{.}$) and root-mean-square (rms) for all presented variables. It is carried out during more than 40 (large eddy) outer time scales $t^* = L_z/W^*$, where $W^* = (BL_z)^{1/3}$ is the convective velocity and $B = \beta g Q / \rho c_p$ is the buoyancy flux. This corresponds to more than 500 inner time scales $t^+ = (\upsilon/B)^{1/2}$ [6]. The inner and outer scales refer to processes in the diffusive boundary layer and mixing layer, respectively. The flow is assumed to be periodic for all variables in the surface-parallel directions, resulting in statistical properties that only depend on the z direction. The horizontal time-space average during the sampling time t_A denoted $\langle . \rangle$ is defined by

$$\langle g \rangle(z) = \frac{1}{t_A} \int_t^{t+t_A} \left(\frac{1}{L_x L_y} \int_0^{L_x} \int_0^{L_y} g(x, y, z, t) dx dy \right) dt. \quad (6)$$

4. Results and discussion

4.1. Enhanced scalar flux due to decreased diffusive boundary layer thickness

Figure 3 shows a snapshot of the temperature field, the surface water velocities, the horizontal flow divergence, $\gamma = \partial u/\partial x + \partial v/\partial y$, and the surface-normal scalar transport, $F_s = -D\, \partial s/\partial z$, at the surface. It is shown in Figure 3a that the cooling of the surface creates cooler denser surface water that, due to instability, eventually forms thin descending plumes of cold denser water (sketched schematically with pale blue arrows). This cold water is replaced by warmer water ascending from the bulk in order to satisfy continuity. The descending cold water and the ascending warm water create the typical temperature field structures (Figures 2 and 3). It also causes straining (sketched schematically with yellow arrows) resulting in a thinner diffusive boundary layer and divergent and convergent regions at the surface. The thin diffusive boundary layer, δ_W, defined as where only 5% of the scalar transport is diffusive and the rest is advective, has been magnified 5 times in relation to the horizontal directions in

Figure 3b. The "islands" that can be seen to protrude the mean diffusive boundary layer, $\bar{\delta}_W \approx 5$ mm for the *Base* case, is the momentary diffusive boundary layer thickness. This momentary diffusive boundary layer thickness is also schematically drawn in red in Figure 1b. It is apparent in Figure 3b-c that there is a strong correlation between δ_W, the surface temperature, and the horizontal divergence. It is also shown in Figure 3b,d that wherever there is an "island" there is also an enhanced scalar flux through the surface, which is due to the increased scalar concentration gradient for thinner diffusive boundary layers.

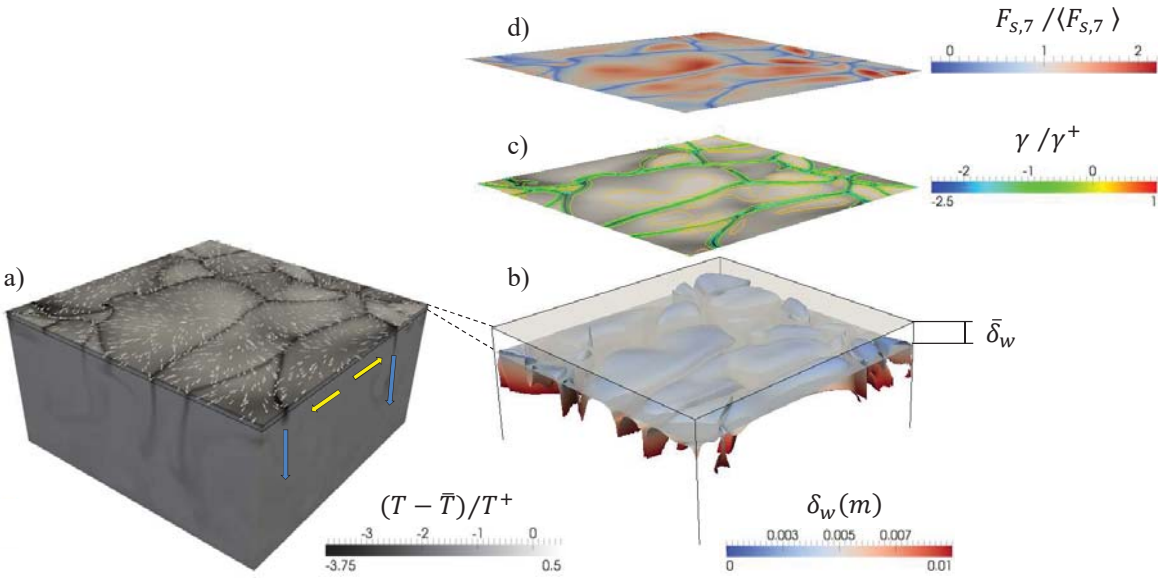

Figure 3. Snapshot, for the *Base* case, of a) the temperature field and the surface water velocities, b) the diffusive boundary layer depth, c) the horizontal flow divergence at the surface and d) the surface-normal scalar transport at the surface.

4.2. Different surface heat fluxes

Figure 4 shows the normalized temperature fields for different surface heat fluxes while keeping the domain size constant. It is interesting to find suitable normalization scales to describe the flow because these scales can be used to investigate, describe and predict other similar flow cases. Fredriksson et al. [6] discuss the use of inner and outer scales thoroughly, where the inner scales are used close to the surface, inside the diffusive boundary layer, and the outer scales are used in the mixed layer outside the diffusive boundary layer. Figure 4 shows that the scale of the thermal structures at the surface decreases with increasing heat flux as is expected according to the inner length scale $L^+ = Pr^{n-1}(\upsilon^3/B)^{1/4}$, where the buoyancy flux B is proportional to the heat flux. This length scale is further affected by Pr and the contamination of the surface, via the exponent n, typically between $1/2$ and $2/3$. The inner length scale is finally affected by the viscosity, but notably not the domain depth. The equivalent length scales for a scalar or a gas is $L^+ = Sc^{n-1}(\upsilon^3/B)^{1/4}$. Note, however, that the decrease in L^+ for gases with large Sc numbers is not reflected in the size of the temperature cells seen in Figure 4 but rather in the concentration gradients near the surface and the diffusive boundary layer thickness. The strong correlation between the inverse diffusive boundary layer thickness and the scalar flux seen in Figure 3 combined with the above expression for a typical vertical length scale leads to a scalar and gas transfer velocity that is proportional to $Q^{1/4}$, as confirmed by Fredriksson et al. [7].

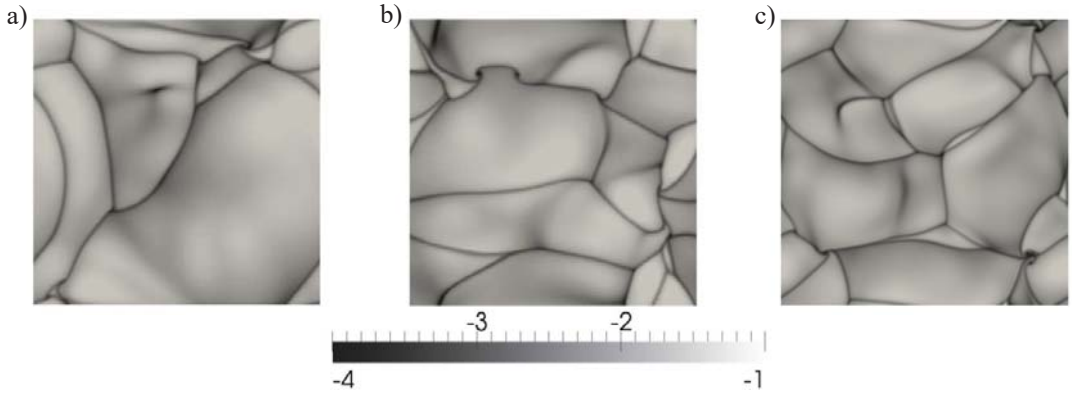

Figure 4. The normalised temperature field $(T-\bar{T})/T^+$ for *Low* a), *Base* b), and *High* c) surface heat flux, where the inner temperature scale $T^+ = QPr^n(Bv)^{-1/4}$.

4.3. Different temperature and scalar concentration profiles

The different boundary conditions for gas (modelled as a passive scalar) and temperature was presented in section 3. Figures 5 and 6 show the resulting concentration and temperature profiles in two different ways, where Figure 5 shows the minimum, mean, maximum, and momentary profiles along the y-z plane in the x-direction and Figure 6 shows the mean and the rms values for the complete sampling period normalised with the inner scaling T^+ and $s^+ = F_s Sc^n (Bv)^{-1/4}$ [6]. It can be seen in Figure 5 that the scalar concentration is constant at the surface but the variation width increases with increasing depth while the variation width is fairly constant for the temperature all the way up to the surface. This is also shown in Figure 6 with s_{rms} and T_{rms} equal to zero and non-zero, respectively, at the surface. It can also be seen in Figure 6 that the scaled s_{rms} and T_{rms} become similar as the depth of the diffusive layer is approached. The gradient of the mean non-dimensional scalar concentration and temperature are similar, although the somewhat smaller gradient for temperature compared to the scalar concentration indicates that the transfer velocity is higher for the heat than the scalar.

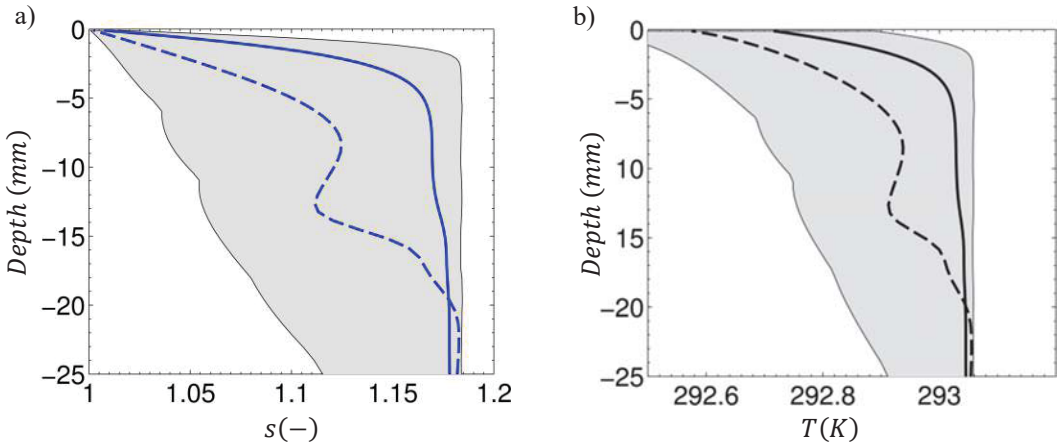

Figure 5. The a) scalar concentration and b) temperature profiles of the flow field in Figure 2 in the y-z plane for $y = 0$. The grey surfaces give the variations with the thin lines indicating the minimum and the maximum values. The dashed lines are the momentary profiles (in the present plot $x = L_x, y = 0$) and the thick lines are the mean value from the profiles for $0 < x < L_x, y = 0$.

The skewed distributions below the surface (Figure 5), with small minimum values compared to mean and max values, are caused by the descending plumes, and the increase in minimum scalar concentration and temperature with depth must therefore be caused by entrainment of ambient water into the plume.

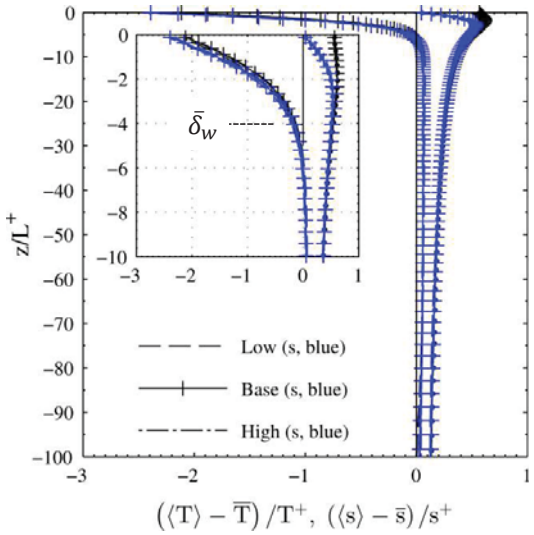

Figure 6. The mean and root-mean-square, normalized by inner scaling, of the fluctuating temperature, $(\langle T\rangle - \bar{T})$, and T_{rms} in black, and the fluctuating scalar concentration, $(\langle s\rangle - \bar{s})$, and s_{rms} in blue. The approximate mean diffusive boundary depth, $\bar{\delta}_w$, is indicated in the inset.

5. Summary

DNS is used to study gas flux across the air-water interface. The flow is driven by natural convection applied as a fixed surface heat flux and the gas transfer is modelled through a passive tracer (scalar concentration) transfer. The present paper discusses some of the results in the full DNS study presented in Fredriksson et al. [6], where the influence of a clean and a surfactant-laden surface as well as the Schmidt number dependence of the gas transfer velocity were studied. Fredriksson et al. [6] performed extensive mesh and domain size sensitivity analyses in order to verify that the results are robust and converged. In the case of a clean surface, modelled with a slip boundary condition, the buoyancy flux dependence was studied by altering the surface heat flux.

The DNS approach is shown to be powerful to enhance the understanding of the gas-transfer during natural convection. The use of inner scaling has been shown to synthesize the results in order to use the results for predicting similar flow cases. It is further illustrated that the momentary gas flux through the surface is closely related to the surface-normal diffusive boundary layer thickness, the temperature and the horizontal flow divergence field at the surface.

Acknowledgments

The computations were performed on resources provided by the Swedish National Infrastructure for Computing (SNIC) at C3SE (Chalmers Centre for Computational Science and Engineering) computing resources. We also acknowledge one anonymous reviewer.

References

[1] Bade D L 2009 Gas exchange at the air–water interface *Encyclopedia of Inland Waters* Likens G E, ed (Oxford: Academic Press) 70
[2] Macintyre S *et al* 2002 The critical importance of buoyancy flux for gas flux across the air-water interface *Gas Transfer at Water Surfaces* (American Geophysical Union) 135
[3] Bastviken D *et al* 2011 *Science* **331** 50
[4] Ciais P *et al* 2013 Carbon and other biogeochemical cycles *Climate Change 2013: The Physical Science Basis. Contribution of Working Group I to the Fifth Assessment Report of the Intergovernmental Panel on Climate Change* (Cambridge University Press)
[5] Tranvik L J *et al* 2009 *Limnol. Oceanogr*. **54** 2298
[6] Fredriksson S T *et al* 2015 An evaluation of gas transfer velocity parameterizations using DNS *J. Geophys. Res*. **Submitted**
[7] Jahne B and Haussecker H 1998 *Ann. Rev. Fluid Mech*. **30** 443
[8] Don W G and Robert H P 2008 Transport Properties *Perry's Chemical Engineers' Handbook, Eighth Edition* (McGraw Hill Profesional)
[9] Kundu P K *et al Fluid Mechanics, 5th ed* (Oxford, UK: Elsevier)
[10] Versteeg H K and Malalasekera W 2007 *An Introduction to Computational Fluid Dynamics: The Finite Volume Method, 2nd ed* (New York: Pearson Education Ltd)